Geomechanics and Engineering, *Vol. 36, No. 4 (2024) 355-366*
https://doi.org/10.12989/gae.2024.36.4.355

Generalization and implementation of hardening soil constitutive model in ABAQUS code

Bo Song[a], Jun-Yan Liu, Yan Liu* and Ping Hu

School of Civil Engineering and Architecture, University of Jinan,
336 Nanxinzhuangxi Rd, Shizhong District, Jinan 250022, China

(*Received August 13, 2023, Revised December 1, 2023, Accepted January 5, 2024*)

Abstract. The original elastoplastic Hardening Soil model is formulated actually partly under hexagonal pyramidal Mohr-Coulomb failure criterion, and can be only used in specific stress paths. It must be completely generalized under Mohr-Coulomb criterion before its usage in engineering practice. A set of generalized constitutive equations under this criterion, including shear and volumetric yield surfaces and hardening laws, is proposed for Hardening Soil model in principal stress space. On the other hand, a Mohr-Coulumb type yield surface in principal stress space comprises six corners and an apex that make singularity for the normal integration approach of constitutive equations. With respect to the isotropic nature of the material, a technique for processing these singularities by means of Koiter's rule, along with a transforming approach between both stress spaces for both stress tensor and consistent stiffness matrix based on spectral decomposition method, is introduced to provide such an approach for developing generalized Hardening Soil model in finite element analysis code ABAQUS. The implemented model is verified in comparison with the results after the original simulations of oedometer and triaxial tests by means of this model, for volumetric and shear hardenings respectively. Results from the simulation of oedometer test show similar shape of primary loading curve to the original one, while maximum vertical strain is a little overestimated for about 0.5% probably due to the selection of relationships for cap parameters. In simulation of triaxial test, the stress-strain and dilation curves are both in very good agreement with the original curves as well as test data.

Keywords: ABAQUS; hardening soil model; isotropic material; Mohr-Coulomb criterion; principal stress space; spectral decomposition

1. Introduction

Derived from the famous hypoelastic Duncan-Chang hyperbolic constitutive model, the elastoplastic Hardening Soil (HS) model introduced by Schanz *et al.* (1999), is a builtin constitutive model in finite element analysis (FEA) code Plaxis (Bentley Systems Inc. 2022), as well as ZSoil and Midas (Kawa *et al.* 2021), and has been widely utilized in a number of geotechnical numerical analyses (Sukkarak *et al.* 2017, Kawa *et al.* 2021, Sukkarak *et al.* 2021). Elastic unloading and reloading behavior is introduced in HS model so as to overcome the theoretical defect of its hypoelastic Duncan-Chang counterpart. This advanced model is formulated under Mohr-Coulomb failure criterion, and is additionally introduced a cap-type yield surface to adapt to the probable situation of volumetric plastic straining in isotropic or nearly isotropic compression.

Unfortunately, in principal stress space, the spatial shape of a deviatorically hardened Mohr-Coulomb type yield surface is a hexagonal pyramid, comprising six corners and an apex (Fig. 1) which cannot be differentiated as regular approaches do (de Souza Neto *et al.* 2008, Wang 2020). This is why Benz (2007) additionally enhanced his HS-Small model, an improved version of HS model featuring larger elastic shear stiffness within small shear strain range, by means of smooth Matsuoka-Nakai failure criterion (Matsuoka and Nakai 1985) which is second-order differentiable (Fig. 2). Besides the alternation of failure criterion, various smoothing methods at the corners as well as the apex (Zienkiewicz and Pande 1977, Menetrey and Willam 1995, Jia *et al.* 2010, Abbo *et al.* 2011, Lester and Sloan 2018, Wang 2020, Amat *et al.* 2023) are also common, with Zienkiewicz and Jia's approaches invoked by Sui *et al.* (2021) for seismic numerical analysis for tunnels, and Abbo's hyperbolic approach well implemented in analyses involving Mohr-Coulomb type yield surfaces, for example Argani and Gajo (2021) and Woo (2023). However, these smoothing approaches can hence underestimate the actual triaxial strength of soil, where the stress state is just on the corner. Another approach to remove these singularities is introduced by Mahetaji *et al.* (2023), by means of introducing weights for three principal stresses in rock analysis.

Sometimes the analysis needs accuracy for both biaxial and triaxial cases. In this situation, the original Mohr-Coulomb surface cannot be smoothed at both corners and apex, so Koiter's rule comes to play (Koiter 1953, Schanz *et al.* 1999, de Souza Neto *et al.* 2008). By returning the trial stress state along their gradients, this rule is troubleshooting

*Corresponding author, Professor
E-mail: liuyan322@163.com
[a]Ph.D. Candidate
E-mail: 1024552201@qq.com

ISSN: 2005-307X (Print), 2092-6219 (Online)

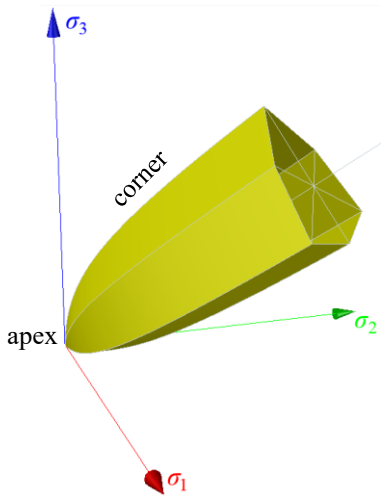

Fig. 1 Pyramidal yield surface of Hardening Soil model for cohesionless soil

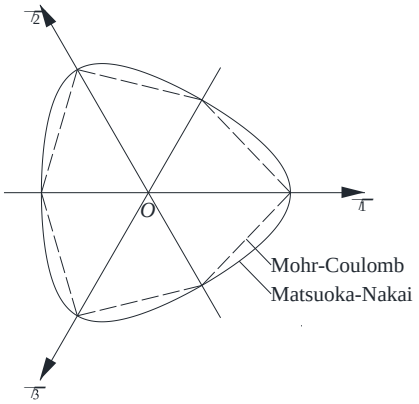

Fig. 2 Yield loci under Mohr-Coulomb and Matsuoka-Nakai criteria on deviatoric plane (Matsuoka and Nakai 1985)

at the singularity curve or point between two or three analytical surfaces respectively, and is widely used to process the corner singularities in Tresca (Zhang *et al.* 2019), Mohr-Coulomb and Hoek-Brown (Li 2021a, b) criteria. In Benz's PhD thesis (2007) he also briefly mentioned the corner and apex problems to be solved with this rule in Mohr-Coulomb type yield surface.

By far the Hardening Soil model is implemented and built in only in a few finite element codes as aforementioned, as well as implemented by Wang *et al.* (2014) in finite difference code FLAC3D. Unfortunately, it is not a builtin constitutive model in the general finite element analysis code ABAQUS (Dassault Systemes Simulia Corp. 2019). This predicament may restrict both its practical and academic utilization, especially involving any of potential complex contact conditions for example between soil and piles (Wu and Vanapalli 2022). Some literature reports various modification and simplification of the original HS model, mainly to vanish the singularities for implementation. Wang *et al.* (2014) assumes that the primary loading behavior is controlled by hyperbolic tangential modulus (actually para-elastic), and the resilience stiffness Eur is adopted to describe the unloading and reloading behavior. On the other hand Pramthawee *et al.* (2011) and Sukkarak *et al.* (2017, 2018) simply substituted the deviatoric stress $\sigma_1 - \sigma_3$ by Roscoe stress invariant q for the settlement analysis of high rockfill dams.

As the original Hardening Soil model is actually not formulated in generalized form and exists such singularities and intersections between shear and volumetric yield surfaces which can cause difficulties in its implementation, the purpose of this paper is to propose a more generalized form of this model with respect to hexagonal Mohr-Coulomb failure criterion, implement the model via ABAQUS's User MATerial (UMAT) subroutine interface, and verify it in element test with data in Schanz *et al.* (1999).

2. Conventions

Throughout this paper, compressive direct stress and strain are considered positive. The nth sextant of deviatoric stress space (n = 1,2,...,6) is defined as the range of Lode angle θ between $\frac{(n-1)\pi}{3}$ and $\frac{n\pi}{3}$ with θ defined as an arccosine function here

$$\theta = \frac{1}{3}\arccos\frac{27J_3}{2q^3} \tag{1}$$

where J_3 and q denote the third deviatoric stress invariant and Roscoe deviatoric stress respectively. $0 \le \theta \le 60°$ holds in the default ranking of principal stress components $\sigma_1 \ge \sigma_2 \ge \sigma_3$. A principal stress or strain tensor is called ranked when its components are in this ranking, and semi-ranked in plane strain and axisymmetric cases when the third component is the out-of-plane component, and the first and second are major and minor in-plane ones respectively. In spatial case a principal stress tensor will be always ranked.

The square brackets [] and braces {} denote the matrix and vector form of a tensor, or the content of a matrix and of a vector, respectively. The bar ¯ marked atop a symbol of stress denotes that $c\cot\varphi$ is added to it, for example $\bar{p} = p + c\cot\varphi$.

3. Generalized formulation of Hardening Soil model

The Hardening Soil model comprises eleven parameters whose symbols used in this paper, $E_{50}^{\mathrm{ref}}, E_{\mathrm{oed}}^{\mathrm{ref}}, E_{\mathrm{ur}}^{\mathrm{ref}}, \nu, c, \varphi, \psi, m, k_0^{\mathrm{nc}}, R_{\mathrm{f}}$, and p^{ref}, are defined in Schanz *et al.* (1999) and will not be re-described here.

The elastic Hardening Soil model assumes that the material is isotropic. According to Peric and de Souza Neto (1999), de Souza Neto *et al.* (2008) and Zhang *et al.* (2019), for plastic correction of an isotropic material, whenever a plastic potential function (or definition of plastic flow tensor) g_i is isotropic for stress tensor σ, its gradient, $\left(\frac{\partial g_i}{\partial \boldsymbol{\sigma}}\right)_{n+1}$, shares the same principal direction with the final

stress state tensor σ^{n+1}, hence as well as trial stress tensor $\boldsymbol{\sigma}_{n+1}^{\text{trial}}$. This results in that the integration of constitutive equations can be simply performed in principal stress space. De Souza Neto *et al*. (2008)'s technique of spectral decomposition transforms a six-dimensional Cauchy stress or strain tensor into principal stress space by solving eigenvalue and eigenprojection problem. A simple matrix multiplication between eigenprojection matrix and eigenvalue vector brings the stress state back to Cauchy stress tensor right after the integration process. Based on this, the generalized formulation of the Hardening Soil model can now be formulated in principal stress space.

3.1 Original formulation

The Hardening Soil model comprises two parts: a pyramid-type yield surface and a cap-type yield surface. Both yield surfaces are analytically shaped under Mohr-Coulomb criterion. A Mohr-Coulomb type yield surface actually consists of six analytical cylindrical portions (Fig. 1), each formulated by different sequences of three principal stresses. Schanz's original formulation of pyramid-type yield function is also formulated in principal stress space, corresponding to two adjacent portions in the yield surface

$$\begin{cases} f_{13} = \dfrac{q_{\text{a}}}{E_{50}} \dfrac{(\sigma_1 - \sigma_3)}{q_{\text{a}} - (\sigma_1 - \sigma_3)} - \dfrac{2(\sigma_1 - \sigma_3)}{E_{\text{ur}}} - \gamma^{\text{p}} \\ f_{12} = \dfrac{q_{\text{a}}}{E_{50}} \dfrac{(\sigma_1 - \sigma_2)}{q_{\text{a}} - (\sigma_1 - \sigma_2)} - \dfrac{2(\sigma_1 - \sigma_2)}{E_{\text{ur}}} - \gamma^{\text{p}} \end{cases} \tag{2}$$

where the subscript 13 denotes the portion in the first sextant of deviatoric stress space where three principal stress components are in default ranking $\sigma_1 \geq \sigma_2 \geq \sigma_3$, and the subscript 12 denotes one of two adjacent portions where $\sigma_1 \geq \sigma_3 \geq \sigma_2$, hence supplementary in case of triaxial compression where $\sigma_1 \geq \sigma_2 = \sigma_3$; q_a is the asymptotic deviatoric stress, E_{50} is secant modulus where deviatoric stress reaches half of ultimate strength, E_{ur} is unloading-reloading modulus or Young's modulus, and γ^p denotes the total generalized plastic shear strain, which originally follows the incremental equation below

$$\mathrm{d}\gamma^{\text{p}} = \mathrm{d}\varepsilon_1^{\text{p}} - \mathrm{d}\varepsilon_2^{\text{p}} - \mathrm{d}\varepsilon_3^{\text{p}} \tag{3}$$

where ε_i^{p} denotes plastic principal strain tensor. The asymptotic deviatoric stress q_{a} is derived after Mohr-Coulomb failure criterion

$$q_{\text{a}} = \frac{2\sin\varphi}{R_{\text{f}}(1-\sin\varphi)} \bar{\sigma}_3 \tag{4}$$

and both stiffness moduli E_{50} and E_{ur} are scaled from their corresponding input reference values by means of minor principal stress

$$\{E_{50}, E_{\text{ur}}\} = \{E_{50}^{\text{ref}}, E_{\text{ur}}^{\text{ref}}\} \left(\frac{\bar{\sigma}_3}{\bar{p}^{\text{ref}}} \right)^m \tag{5}$$

With Rowe's theory of dilatancy utilized to evaluate the plastic flow in material, a non-associative plastic flow rule is adopted in the Hardening Soil model, but it is not described by an explicit plastic potential function. According to the equation of Rowe's theory

$$\mathrm{d}\varepsilon_v^p = \sin\psi_m \mathrm{d}\gamma^p \tag{6}$$

the hardening law of Hardening Soil model is written with assistance of Koiter's rule in Schanz's original work

$$\begin{aligned} \{\mathrm{d}\varepsilon_i^{\text{p}}\} = {} & \mathrm{d}\lambda_{13} \left\{ \frac{1+\sin\psi_m}{2}, 0, \frac{-1+\sin\psi_m}{2} \right\}^T \\ & + \mathrm{d}\lambda_{12} \left\{ \frac{1+\sin\psi_m}{2}, \frac{-1+\sin\psi_m}{2}, 0 \right\}^T, \end{aligned} \tag{7}$$

where $\sin\psi_{\text{m}}$ is mobilized dilation angle

$$\sin\psi_{\text{m}} = \frac{\sin\varphi_{\text{m}} - \sin\varphi_{\text{cv}}}{1 - \sin\varphi_{\text{m}} \sin\varphi_{\text{cv}}} \tag{8}$$

defined by mobilized friction angle

$$\sin\varphi_{\text{m}} = \frac{\bar{\sigma}_1 - \bar{\sigma}_3}{\bar{\sigma}_1 + \bar{\sigma}_3} \tag{9}$$

and constant critical-state friction angle

$$\sin\varphi_{\text{cv}} = \frac{\sin\varphi - \sin\psi}{1 - \sin\varphi \sin\psi} \tag{10}$$

The associated cap-type yield surface in Hardening Soil model is described as

$$f^c = g^c = \frac{\tilde{q}^2}{M^2} + \bar{p}^2 - \bar{p}_c^2 \tag{11}$$

where $\tilde{q} = \sigma_1 + (\alpha - 1)\sigma_2 - \alpha\sigma_3$ is another type of deviatoric stress measure adapted to the deviatoric shape of Mohr-Coulomb locus, with constant $\alpha = \dfrac{3+\sin\varphi}{3-\sin\varphi}$; p is mean stress or hydrostatic pressure, and p_{c} denotes pre-consolidation pressure that plays a role of volumetric hardening parameter

$$\mathrm{d}p_{\text{c}} = H \mathrm{d}\varepsilon_{\text{v}}^{\text{p}} \tag{12}$$

where $\varepsilon_{\text{v}}^{\text{p}}$ denotes plastic volumetric strain, and H is hardening modulus derived from elastic bulk modulus K and elastoplastic compression modulus K_{c}:

$$H = \frac{KK_{\text{c}}}{K - K_{\text{c}}} = \frac{K}{K/K_{\text{c}} - 1} \tag{13}$$

Schanz *et al.* did not propose certain equations for cap parameters M and H, but figured out that they are related to input parameters k_0^{nc} and $E_{\text{oed}}^{\text{ref}}$. Many such relationships are reported in literature (Surarak *et al.* 2012, Wang *et al.* 2014, Pramthawee *et al.* 2017), for example (Wang *et al.* 2014)

$$M = \frac{6\sin\varphi}{3-\sin\varphi}, K_c = \frac{1+2k_0^{\text{nc}}}{3} E_{\text{oed}}^{\text{ref}} \left(\frac{\bar{\sigma}_1}{\bar{p}^{\text{ref}}} \right)^m \tag{14}$$

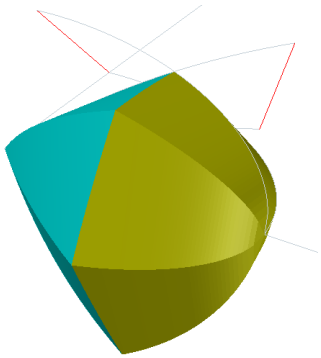

Fig. 3 The spatial shape of shear (cyan) and cap (yellow) yield surfaces of Hardening Soil model in principal stress space, with red lines representing the generatrices of cylindrical parts in both yield surfaces

and (Plaxis, Bentley Systems Inc. 2022)

$$M = k_0^{\mathrm{nc}}, H = \frac{K^{\mathrm{ref}}}{K / K_{\mathrm{c}} - 1}\left(\frac{\bar{p}_{\mathrm{p}}}{\bar{p}^{\mathrm{ref}}}\right)^m \tag{15}$$

where $K^{\mathrm{ref}} = \dfrac{E_{\mathrm{ur}}^{\mathrm{ref}}}{3(1-2\nu)}$, and modulus ratio

$$\frac{K}{K_{\mathrm{c}}} = \frac{E_{\mathrm{ur}}^{\mathrm{ref}}}{E_{\mathrm{oed}}^{\mathrm{ref}}} \frac{k_0^{\mathrm{nc}}}{(1+2k_0^{\mathrm{nc}})(1-2\nu)} \tag{16}$$

The cap-type yield surface is plotted with pyramidal shear yield surface in Fig. 3.

3.2 Generalization

Schanz's original yield functions can actually only describe the material behavior in triaxial compression case as Duncan-Chang model does because they are not completely generalized, for example, minor principal stress component σ_3 is involved in f_{12} and its hardening law, and shear hardening parameter γ^p actually includes volumetric part and is hence not fully deviatoric (Eq. (3)). Therefore, the original Hardening Soil model is to some extent violating Mohr-Coulomb failure criterion, where a set of shear yield functions actually involves two principal stress components in each deviatoric sextant. Before the model can be used for any stress path that may appear in engineering practice, it must be completely generalized under Mohr-Coulomb criterion. This generalization approach is completely different from Plaxis's method (Bentley Systems Inc. 2022), with the general deviatoric stress measure q defined by major principal strain component ε_1.

As the equations of both f_{12} and its plastic flow vector (the vector multiplied by $d\lambda_{12}$ in Eq. (7)) are supplementary for triaxial compression case where $\sigma_1 > \sigma_2 = \sigma_3$, the moduli E_{50} and E_{ur} in f_{12} are considered to be scaled by σ_2 instead of σ_3. The volumetric part in incremental plastic shear strain $d\gamma^p$ is actually equal to zero according to Eq. (7) for flow rule. In plastic flow vector σ_2 is also used instead of σ_3 to calculate mobilized dilation angle sin ψ_m. As a result, the yield function f_{12} and its plastic flow vector become totally independent of σ_3. With respect to the order of two principal stress components in each deviatoric sextant, the generalized constitutive equations of Hardening Soil model for shear hardening can be built as

$$f^{\mathrm{S}}(\sigma_a, \sigma_b, \gamma^{\mathrm{p}}) = \frac{q_a(\sigma_b)}{E_{50}(\sigma_b)} \frac{\sigma_a - \sigma_b}{q_a(\sigma_b) - (\sigma_a - \sigma_b)} - \frac{2(\sigma_a - \sigma_b)}{E_{ur}(\sigma_b)} - \gamma^{\mathrm{p}}, \tag{18}$$

$$m_a^{\mathrm{S}} = \frac{1+\sin\psi_m}{2}, m_b^{\mathrm{S}} = \frac{-1+\sin\psi_m}{2}, m_c^{\mathrm{S}} = 0 \tag{19}$$

where $a, b, c = 1, 2, 3, a \neq b, b \neq c, c \neq a$. The plastic flow tensor (vector) $m_i^{\mathrm{S}}(\sigma_a, \sigma_b)$ indicates the direction of plastic flow onto its corresponding analytic portion of yield surface $f^{\mathrm{S}}(\sigma_a, \sigma_b, \gamma^{\mathrm{p}})$, with the modified definition of $\sin\psi_m(\sigma_a, \sigma_b) = \dfrac{\bar{\sigma}_a - \bar{\sigma}_b}{\bar{\sigma}_a + \bar{\sigma}_b}$.

According to the order of principal stress components for each shear yield function in the set, the set of yield functions for volumetric hardening can be easily interpreted as

$$f^{\mathrm{C}}(\sigma_a, \sigma_b, \sigma_c, p_c) = \left(\frac{\sigma_a + (\alpha-1)\sigma_b - \alpha\sigma_c}{M}\right)^2 + \bar{p}^2 - \bar{p}_c^2 \tag{20}$$

where $p = \dfrac{\sigma_a + \sigma_b + \sigma_c}{3}$ again denotes mean stress which is an invariant. For volumetric hardening

$$m_i^{\mathrm{C}}(\sigma_a, \sigma_b, \sigma_c) = \frac{\partial f^{\mathrm{C}}(\sigma_a, \sigma_b, \sigma_c)}{\partial \sigma_i} \tag{21}$$

simply holds.

As aforementioned, only in case of triaxial compression does Eq. (3) hold for incremental plastic shear strain $\mathrm{d}\gamma^p$ since the model is directly derived from Duncan-Chang model. In case of triaxial extension $\mathrm{d}\gamma^p = \mathrm{d}\varepsilon_1^{\mathrm{p}} + \mathrm{d}\varepsilon_2^{\mathrm{p}} - \mathrm{d}\varepsilon_3^{\mathrm{p}}$ actually holds instead of Eq. (3), with volumetric part also equal to zero. In any case of load this measure should be equal to the only shear plastic multiplier or the sum of two shear plastic multipliers since $m_a^{\mathrm{S}} - m_b^{\mathrm{S}} \equiv 1$ according to the definition in Eq. (19). In case of double hardening the product between volumetric plastic multiplier and

$$\omega = \frac{2\tilde{q}}{M^2}\sqrt{3(\alpha^2 - \alpha + 1)} \tag{22}$$

should be also added. Eq. (22) is formulated after the equation of generalized plastic deviatoric strain $\varepsilon_{\mathrm{d}}^{\mathrm{p}}$.

4. Plan of ABAQUS user subroutine interface UMAT

Because Newton-Raphson iteration method is utilized by the implicit finite element analysis solver in ABAQUS code, the mission of its UMAT subroutine interface is to

Table 1 Plan of ABAQUS user subroutine UMAT for generalized Hardening Soil model

No.	Module name	Components
1	mod_hs_basic	Necessary and optional input parameters Other constants Pointers to state-dependent variables (DepVar) A subroutine for initializing variables above Yield functions
2	mod_hs_rm	Subroutines of implicit return mapping algorithms in different cases of hardening
3	mod_hs_bm	Subroutines for building 3×3 consistent stiffness matrix in ranked principal stress space
4	mod_hs_main	Subroutine for stress updating Subroutine for assembling consistent stiffness matrix in Cauchy stress space The main subroutine invoked by UMAT
5	UMAT: use mod_hs_main; include SDVINI for initializing state variables	

update the stress tensor at the end of time increment step, and assemble the consistent algorithmic elastoplastic stiffness matrix for global iteration. The UMAT code in this paper is programmed in modern Fortran language, only remaining in the fixed form of FORTRAN77, so modules are introduced to manage the framework of UMAT. A module can use the member variables, functions and subroutines from other modules via a USE statement at the head of module code. The main framework of UMAT is therefore divided into four main modules in order below, shown in Table 1, where one module or final UMAT uses its preceding module.

Because the material is isotropic, in any case of plastic correction step both eigendirections of principal stress and principal strain tensors keep fixed, i.e., the stress and total strain tensors share one set of fixed principal directions, according to Zhang *et al.* (2019). With the help of spectral decomposition, the eigensystem of Cauchy stress or strain tensor is found. It should be therefore possible to transform the final consistent stiffness matrix from principal stress space to generalized Cauchy stress space (with dimensions 4×4 in plane strain and axisymmetric cases and 6×6 in spatial case). For algorithmic details for spectral decomposition and transforming of final consistent stiffness matrix, see de Souza Neto *et al.* (2008). These methods are organized in an additional utility module used by "mod_hs_main."

Due to the convention of positive compressive stress, stress, strain and incremental strain tensors must be negated before the main subroutine is invoked in UMAT, and after the end of main subroutine they must be negated again.

In the implementation of Hardening Soil model in ABAQUS code, five input parameters are actually optional and set default values, which are

$$\left.\begin{aligned} &k_0^{\mathrm{nc}} = 1-\sin\varphi, && \text{(Jaky 1944)}\\ &\nu = \frac{k_0^{\mathrm{nc}}}{1-k_0^{\mathrm{nc}}}, &&\\ &\psi = \max(\varphi-30°, 0), && \text{(Bolton 1986)}\\ &R_{\mathrm{f}} = 0.9, && \text{and}\\ &p^{\mathrm{ref}} = 100\ \mathrm{kPa} && \end{aligned}\right\} \tag{23}$$

and Wang's definition for cap parameters M and H is used. The number of state-dependent variables (DepVar) is at least two, for both shear and volumetric hardening parameters respectively. This number will increase if any other factor is focused on, for example small strain considerations (Benz 2007). Pointers to each DepVar are defined so as to manipulate these variables directly.

5. Stress updating module

The implicit closest point projection algorithm is used in returning the trial stress state onto yield surface(s). Generally the elastic trial stress state should be returned onto the yield surface to make its corresponding yield function equal to zero at the end of an increment, along the unique direction of plastic flow. However, with Mohr-Coulomb type definition of plastic flow adopted in the generalized Hardening Soil model, there seem to be inconsistent directions of plastic flow at the corners of yield surface which is also of Mohr-Coulomb type, making singularities when directly using common integration approach in Cauchy stress space to solve triaxial load cases. In this situation if any smoothing approach is not recommended, an approach with regard of Koiter's rule is invoked to deal with such kind of singularity. Along their corresponding directions of plastic flow, the stress state will be returned to both main and adjacent cylindrical portions of yield surface, and hence fall on the intersection curve between them, i.e., the corner.

Since the scaling factor for both secant and Young's moduli

$$S = \left(\frac{\bar{\sigma}_3}{\bar{p}_{\mathrm{ref}}}\right)^m \tag{24}$$

becomes meaningless in the range of hydrostatic pressure $p \le -c\cot\varphi$, the stress state will never be returned to the apex of shear yield surface. On the other hand, isotropic loading may cause the final stress state to be returned to the apex of cap-type yield surface, regarding of its elliptic shape on the meridional plane and associated flow rule. In this situation the volumetric yield function is actually reduced to only one equation since deviatoric stress is equal to zero, although three cylindrical portions of cap yield surface are actually involved

$$f^{\mathrm{C}} = p - p_c \tag{25}$$

In summary of the discussion above, up to ten types of hardening may occur and decide the corresponding return mapping scheme during plastic correction process, involving destinations on both main cylindrical surfaces of pyramid and cap, as well as their intersections, corners, and the apex of cap surface (Fig. 4). Each type of hardening is assigned a case number from 1 to 10 in Fortran code, illustrated in Fig. 4, to decide the corresponding matrix building scheme afterwards. Koiter's rule is invoked in all the returning cases to these singularities and intersections (i.e., excluding cases 1 and 4), which will be discussed in next subsections.

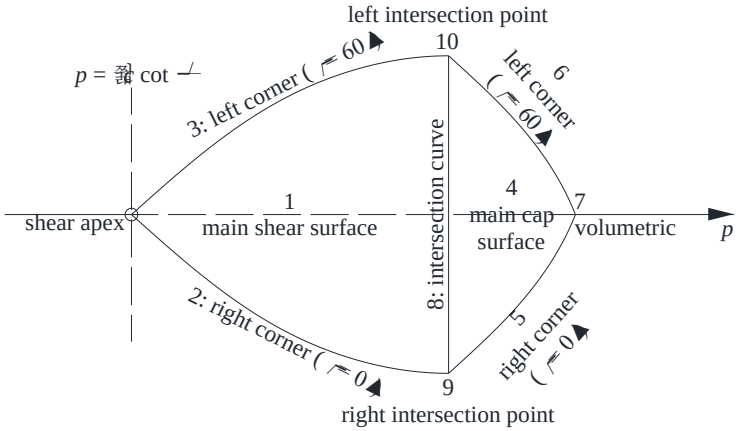

Fig. 4 Return mapping destinations on the main shear and volumetric (cap) yield surfaces of the Hardening Soil model, indicated by case numbers 1 to 10

In stress updating method, elastic prediction for stress tensor is done at first to derive trial stress tensor (usually in the form of a vector), with Young's modulus E_{ur} scaled with initial minor principal stress σ_3. The trial stress tensor is then transformed into principal stress space via spectral decomposition, with first-order principal stress tensor σ_i^{trial} ranked. Both main yield functions, $f^{\text{S}}(\sigma_1^{\text{trial}},\sigma_3^{\text{trial}},\gamma^{\text{p0}})$ and $f^{\text{C}}(\sigma_1^{\text{trial}},\sigma_2^{\text{trial}},\sigma_3^{\text{trial}},p_{\text{c}}^0)$, are calculated to decide which basic type of hardening would occur, where the superscript 0 denotes the state of hardening parameter at the beginning of the current increment. The material is considered hardened if one of these yield functions exceeds a small positive value, called positive tolerance, rather than zero. If the trial stress state is located within the elastic domain, then hardening type 0 is output and the subroutine returns. After plastic correction, the stress tensor is transformed back to Cauchy stress space.

All return mapping schemes are based on the generalized formulation of Hardening Soil model defined in Eqs. (18)-(21).

5.1 Return mapping onto shear surface

If only main shear yield function exceeds its positive tolerance, then the final stress state would be returned onto shear yield surface. At first, the ranked principal stress tensor is attempted to return onto main shear surface

$$\begin{cases} \sigma_i = \sigma_i^{\text{trial}} - b_i \mathrm{d}\lambda^a \\ \{b_i\} = K\sin\psi_{\text{m}} + 2G\left\{\dfrac{1}{2}+\dfrac{\sin\psi_{\text{m}}}{6}, -\dfrac{\sin\psi_{\text{m}}}{3}, -\dfrac{1}{2}+\dfrac{\sin\psi_{\text{m}}}{6}\right\}^T \\ \gamma^{\text{p}} = \gamma^{\text{p0}} + \mathrm{d}\lambda^a \\ f^{\text{S}}(\sigma_1,\sigma_3,\gamma^{\text{p}}) = 0 \end{cases} \tag{26}$$

where $\mathrm{d}\lambda^a$ is plastic multiplier. The final equation in Eq. (26) is solved by means of basic iteration method. In each cycle of iteration, the scaling factor S and mobilized dilation angle $\sin\psi_m$ are frozen and a quadratic equation for $\mathrm{d}\lambda^a$ is finally formulated. The iteration normally ends when the absolute value of yield function falls within its range of tolerance. If the final principal stress tensor is also ranked, then adopt it as well as the updated hardening parameter γ^{p} (case 1 in Fig. 4).

Once the ranking of principal stress components is violated, the yield function for adjacent cylindrical portion will be greater than zero, so the stress state will be returned onto the corner between main and adjacent portions of yield surface, corresponding to triaxial load cases. The situations $\sigma_2 \geq \sigma_1$ and $\sigma_2 \leq \sigma_3$ correspond to triaxial extension and compression, as well as return mapping onto left and right corner of shear yield surface, or case 3 and 2, respectively. Using Koiter's rule one can handily write this formulation derived from Eq. (26) for triaxial compression (case 2)

$$\begin{cases} \sigma_i = \sigma_i^{\text{trial}} - b_i^a \mathrm{d}\lambda^a - b_i^b \mathrm{d}\lambda^b \\ \{b_i^a\} = K\sin\psi_{\text{m}} + 2G\left\{\dfrac{1}{2}+\dfrac{\sin\psi_{\text{m}}}{6}, -\dfrac{\sin\psi_{\text{m}}}{3}, -\dfrac{1}{2}+\dfrac{\sin\psi_{\text{m}}}{6}\right\}^T \\ \{b_i^b\} = K\sin\psi_{\text{m}} + 2G\left\{\dfrac{1}{2}+\dfrac{\sin\psi_{\text{m}}}{6}, -\dfrac{1}{2}+\dfrac{\sin\psi_{\text{m}}}{6}, -\dfrac{\sin\psi_{\text{m}}}{3}\right\}^T \\ \gamma^{\text{p}} = \gamma^{\text{p0}} + \mathrm{d}\lambda^a + \mathrm{d}\lambda^b \\ f^{\text{S}}(\sigma_1,\sigma_3,\gamma^{\text{p}}) = 0 \\ f^{\text{S}}(\sigma_1,\sigma_2,\gamma^{\text{p}}) = 0 \end{cases} \tag{27}$$

and for triaxial extension (case 3)

$$\begin{cases} \sigma_i = \sigma_i^{\text{trial}} - b_i^a \mathrm{d}\lambda^a - b_i^b \mathrm{d}\lambda^b \\ \{b_i^a\} = K\sin\psi_{\text{m}} + 2G\left\{\dfrac{1}{2}+\dfrac{\sin\psi_{\text{m}}}{6}, -\dfrac{\sin\psi_{\text{m}}}{3}, -\dfrac{1}{2}+\dfrac{\sin\psi_{\text{m}}}{6}\right\}^T \\ \{b_i^b\} = K\sin\psi_{\text{m}} + 2G\left\{-\dfrac{\sin\psi_{\text{m}}}{3}, \dfrac{1}{2}+\dfrac{\sin\psi_{\text{m}}}{6}, -\dfrac{1}{2}+\dfrac{\sin\psi_{\text{m}}}{6}\right\}^T \\ \gamma^{\text{p}} = \gamma^{\text{p0}} + \mathrm{d}\lambda^a + \mathrm{d}\lambda^b \\ f^{\text{S}}(\sigma_1,\sigma_3,\gamma^{\text{p}}) = 0 \\ f^{\text{S}}(\sigma_2,\sigma_3,\gamma^{\text{p}}) = 0 \end{cases} \tag{28}$$

Analogously, the final two equations for $\mathrm{d}\lambda^a$ and $\mathrm{d}\lambda^b$ in Eqs. (27) and (28) can be transformed into quadratic equations in each cycle of iteration by freezing S and $\sin\psi_m$. The set of quadratic equations can be solved by means of Newton- Raphson iteration method.

The legend of this return mapping strategy is concluded in Fig. 5. The tensors $\boldsymbol{N}^a$, $\boldsymbol{N}^b$ denote the directions of return

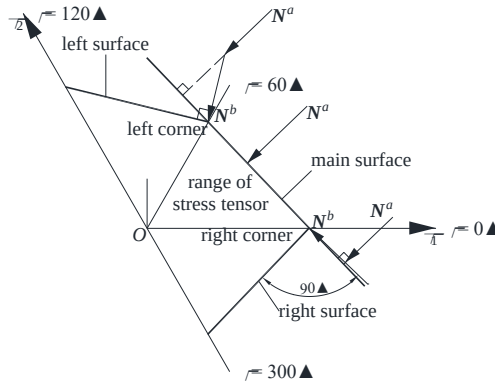

Fig. 5 Return mapping onto main surface, right corner and left corner of Mohr-Coulomb yield surface set, depicted on deviatoric plane

mapping orthogonal to the main surface and right or left surface due to Mohr-Coulomb-type plastic potential, respectively.

5.2 Return mapping onto cap surface

If only the main volumetric yield function $f^{\mathrm{C}}(\sigma_1,\sigma_2,\sigma_3,p_c)$ exceeds its positive tolerance, then return mapping onto cap surface is bound to be done. At first, the magnitude of deviatoric stress measure, $\tilde{q}$, should be checked. If $\tilde{q}$ is negligibly small, then return mapping to the apex of cap-type yield surface (case 7) will be performed using simplified yield function (Eq. (25))

$$\begin{cases} \overline{p} = \dfrac{\overline{p}^{\mathrm{trial}}}{1+2K\mathrm{d}\lambda^c} \\ \overline{p}_{\mathrm{c}} = \overline{p}_{\mathrm{c}0} + 2H\overline{p}\mathrm{d}\lambda^c \\ f^{\mathrm{C}} = \overline{p} - \overline{p}_{\mathrm{c}} = 0 \end{cases} \tag{29}$$

yielding the same value for all three principal stress components. Otherwise, analogous to that onto shear yield surface, the return mapping scheme onto cap-type yield surface also starts with an attempt to return the final stress state onto main cylindrical portion (case 4)

$$\begin{cases} \sigma_i = \sigma_i^{\mathrm{trial}} - b_i\mathrm{d}\lambda^c \\ \{b_i\} = 2G\dfrac{2\tilde{q}}{M^2}\{1,\alpha-1,-\alpha\}^{\mathrm{T}} + 2K\overline{p} \\ p_{\mathrm{c}} = p_{\mathrm{c}0} + 2H\overline{p}\mathrm{d}\lambda^c \\ f^c = f^c(\sigma_1,\sigma_2,\sigma_3,p_{\mathrm{c}}) = 0 \end{cases} \tag{30}$$

Whenever the ranking of intermediate principal stress component σ_2 is altered, the stress state should be finally returned onto one of the corners on the cap, for triaxial compression (returned onto the right corner, case 5)

$$\begin{cases} \sigma_i = \sigma_i^{\mathrm{trial}} - b_i^c\mathrm{d}\lambda^c - b_i^d\mathrm{d}\lambda^d \\ \{b_i^c\} = 2G\dfrac{2\tilde{q}}{M^2}\{1,\alpha-1,-\alpha\}^{\mathrm{T}} + 2K\overline{p} \\ \{b_i^d\} = 2G\dfrac{2\tilde{q}_d}{M^2}\{1,-\alpha,\alpha-1\}^{\mathrm{T}} + 2K\overline{p} \\ p_{\mathrm{c}} = p_{\mathrm{c}0} + 2H\overline{p}(\mathrm{d}\lambda^c + \mathrm{d}\lambda^d) \\ f^{\mathrm{C}}(\sigma_1,\sigma_2,\sigma_3,p_{\mathrm{c}}) = 0 \\ f^{\mathrm{C}}(\sigma_1,\sigma_3,\sigma_2,p_{\mathrm{c}}) = 0 \end{cases} \tag{31}$$

and for triaxial extension (returned onto the left corner, case 6)

$$\begin{cases} \sigma_i = \sigma_i^{\mathrm{trial}} - b_i^c\mathrm{d}\lambda^c - b_i^d\mathrm{d}\lambda^d \\ \{b_i^c\} = 2G\dfrac{2\tilde{q}}{M^2}\{1,\alpha-1,-\alpha\}^{\mathrm{T}} + 2K\overline{p} \\ \{b_i^d\} = 2G\dfrac{2\tilde{q}_d}{M^2}\{\alpha-1,1,-\alpha\}^{\mathrm{T}} + 2K\overline{p} \\ p_{\mathrm{c}} = p_{\mathrm{c}0} + 2H\overline{p}(\mathrm{d}\lambda^c + \mathrm{d}\lambda^d) \\ f^{\mathrm{C}}(\sigma_1,\sigma_2,\sigma_3,p_{\mathrm{c}}) = 0 \\ f^{\mathrm{C}}(\sigma_2,\sigma_1,\sigma_3,p_{\mathrm{c}}) = 0 \end{cases} \tag{32}$$

It is noted that though two quadratic equations for plastic multipliers $\mathrm{d}\lambda^c, \mathrm{d}\lambda^d$ are formulated after Eq. (31) or Eq. (32), a simple equivalence for deviatoric stress can be easily found and reduce one of these equations to a linear equation. As a result, the other one becomes a quadratic equation with actually only one unknown.

5.3 Return mapping onto the intersection between both type of yield surfaces

If both type of yield functions are violated by the trial stress state, then it is expected to perform the return mapping onto the intersection curve (strictly not a line) between both type of yield surfaces (case 8). According to Koiter's rule, it is easy to write the equations for return mapping onto the intersection curve

$$\begin{cases} \sigma_i = \sigma_i^{\mathrm{trial}} - b_i^a\mathrm{d}\lambda^a - b_i^c\mathrm{d}\lambda^c \\ \gamma^{\mathrm{p}} = \gamma^{\mathrm{p}0} + \mathrm{d}\lambda^a + \omega\mathrm{d}\lambda^c \\ p_{\mathrm{c}} = p_{\mathrm{c}0} + H(\sin\psi_m\mathrm{d}\lambda^a + 2\overline{p}\mathrm{d}\lambda^c) \\ f^{\mathrm{S}}(\sigma_1,\sigma_3,\gamma^p) = 0 \\ f^{\mathrm{C}}(\sigma_1,\sigma_2,\sigma_3,p_{\mathrm{c}}) = 0 \end{cases} \tag{33}$$

with the definitions of tensors b_i in Eqs. (27) and (31), and ω in Eq. (22). If the ranking of principal stress components is violated, the final stress state is expected to be returned to one of two intersection points. Each of these intersection points is between four cylindrical surfaces, so it seems that four quadratic equations should be built during each cycle of iteration, and solved by means of Newton-Raphson iteration method, for example to the right intersection point

$$\begin{cases} f^{\mathrm{S}}(\sigma_1,\sigma_3,\gamma^p) = 0 \\ f^{\mathrm{S}}(\sigma_1,\sigma_2,\gamma^p) = 0 \\ f^{\mathrm{C}}(\sigma_1,\sigma_2,\sigma_3,p_{\mathrm{c}}) = 0 \\ f^{\mathrm{C}}(\sigma_1,\sigma_3,\sigma_2,p_{\mathrm{c}}) = 0 \end{cases} \tag{34}$$

However, considering that an intersection point is defined by three cylindrical surfaces that intersect with each other within its vicinity, computational singularity will arise whenever the fourth equation is introduced. This is bound to result in the simplification for return mapping to the right intersection point to make use of three equations and abandon the fourth

$$\begin{cases} \sigma_i = \sigma_i^{\mathrm{trial}} - b_i^a\mathrm{d}\lambda^a - b_i^b\mathrm{d}\lambda^b - b_i^c\mathrm{d}\lambda^c \\ \gamma^{\mathrm{p}} = \gamma^{\mathrm{p}0} + \mathrm{d}\lambda^a + \mathrm{d}\lambda^b + \omega\mathrm{d}\lambda^c \\ p_{\mathrm{c}} = p_{\mathrm{c}0} + H(\sin\psi_m\mathrm{d}\lambda^a + \sin\psi_m\mathrm{d}\lambda^b + 2\overline{p}\mathrm{d}\lambda^c) \\ f^{\mathrm{S}}(\sigma_1,\sigma_3,\gamma^p) = 0 \\ f^{\mathrm{S}}(\sigma_1,\sigma_2,\gamma^p) = 0 \\ f^{\mathrm{C}}(\sigma_1,\sigma_2,\sigma_3,p_{\mathrm{c}}) = 0 \end{cases} \tag{35}$$

for return mapping to the right intersection point (case 9), and for that to the left point (case 10)

$$\begin{cases} \sigma_i = \sigma_i^{\text{trial}} - b_i^a \mathrm{d}\lambda^a - b_i^b \mathrm{d}\lambda^b - b_i^c \mathrm{d}\lambda^c \\ \gamma^{\text{p}} = \gamma^{\text{p0}} + \mathrm{d}\lambda^a + \mathrm{d}\lambda^b + \omega \mathrm{d}\lambda^c \\ p_{\text{c}} = p_{\text{c0}} + H(\sin\psi_m \mathrm{d}\lambda^a + \sin\psi_m \mathrm{d}\lambda^b + 2\bar{p}\mathrm{d}\lambda^c) \\ f^{\text{S}}(\sigma_1, \sigma_3, \gamma^p) = 0 \\ f^{\text{S}}(\sigma_2, \sigma_3, \gamma^p) = 0 \\ f^{\text{C}}(\sigma_1, \sigma_2, \sigma_3, p_{\text{c}}) = 0 \end{cases} \tag{31}$$

6. Stiffness matrix building module

The processes for building or assembling 3×3 elastoplastic stiffness matrix according to hardening type indicator and ranked principal stress tensor in principal stress space are included in the module "mod_hs_bm." It should be paid attention that in plane strain and axisymmetric problems, the assembling process of final consistent elastoplastic stiffness matrix, named DDSDDE in UMAT code, must be based on semi-ranked principal stress and strain tensors yielded from spectral decomposition, with the term *semi-ranked* defined in previous Section 2. In this situation, the 3×3 matrix resulted from "mod_hs_bm" has to be rearranged before the final assembly. One should make the principal stress tensor ranked and note down its original ranking before selecting the matrix building scheme by hardening type indicator. In three-dimensional problems, the principal tensor will be always ranked and this rearranging process vanishes

All matrix building subroutines make use of the elastic stiffness matrix

$$D_{ij} = \lambda + 2G\delta_{ij} \tag{37}$$

where $\lambda = \dfrac{2G\nu}{1-2\nu}$ denotes Lame's elastic constant, $G = \dfrac{E_{ur}}{2(1+\nu)}$ is shear modulus, and the tensor δ_{ij} denotes Kronecker delta.

In hardening cases 1, 4 and 7 defined in Fig. 4, only one yield function is involved in return mapping computation, and the 3×3 matrix is built after the tensorial equation below

$$\frac{\partial \sigma_i}{\partial \varepsilon_j} = \left(\delta_{ik} - \frac{b_i n_k}{X} \right) D_{kj} \tag{38}$$

where $n_i = \dfrac{\partial f}{\partial \sigma_i}, b_i = D_{ij} m_j, X = n_i b_i + A$, with f standing for the sole yield function, m_i being the plastic flow direction vector, h denoting the hardening parameter for shear or volumetric hardening, i.e., γ^{p} or p_{c}, and $A = -\dfrac{\partial f}{\partial h}\dfrac{\partial h}{\partial \mathrm{d}\lambda}$, with $A = 1$ for shear hardening and $A = 4H\overline{pp}_c$ for volumetric hardening after the definition of incremental hardening parameters in the previous Section 5.

In hardening cases 2, 3, 5, 6 and 8 involving two distinct yield functions a and b, the matrix is built after

$$\frac{\partial \sigma_i}{\partial \varepsilon_j} = \left(\delta_{ik} - \frac{u_{bb} b_i^a n_k^a - u_{ab} b_i^a n_k^b - u_{ba} b_i^b n_k^a + u_{aa} b_i^b n_k^b}{u_{aa} u_{bb} - u_{ab} u_{ba}} \right) D_{kj} \tag{39}$$

where

$$u_{\alpha\beta} = n_i^\alpha b_i^\beta + A_{\alpha\beta} \text{ with } \alpha, \beta = a, b \tag{40}$$

with $A_{\alpha\beta} \equiv 1$ for shear hardening cases 2 and 3, $A_{\alpha\beta} = 4H\overline{pp}_c$ for volumetric hardening cases 5 and 6, and

$$\begin{cases} A_{aa} = 1 \\ A_{ab} = \omega \\ A_{ba} = 2H\overline{p}_c \sin\psi_m \\ A_{bb} = 4H\overline{pp}_c \end{cases} \tag{41}$$

for combined hardening case 8.

In double hardening cases 9 and 10, an actually tensorial formulation will be invoked for building the 3×3 matrix

$$\frac{\partial \sigma_i}{\partial \varepsilon_j} = (\delta_{ik} - B_{im} U_{ml} N_{lk}) D_{kj} \tag{42}$$

where

$$B_{ij} = D_{ik} M_{kj} \tag{43}$$

$$[M_{ij}] = \begin{cases} [\{m_i^{\text{S}}\}(\sigma_1, \sigma_3), \{m_i^{\text{S}}\}(\sigma_1, \sigma_2), \{m_i^{\text{C}}\}(\sigma_1, \sigma_2, \sigma_3)] \text{ for triaxial compression} \\ [\{m_i^{\text{S}}\}(\sigma_1, \sigma_3), \{m_i^{\text{S}}\}(\sigma_2, \sigma_3), \{m_i^{\text{C}}\}(\sigma_1, \sigma_2, \sigma_3)] \text{ for triaxial extension} \end{cases} \tag{44}$$

$$N_{ij} = \frac{\partial f_i}{\partial \sigma_j} \tag{45}$$

$$U_{ij} = (N_{ik} B_{kj} + A_{ij})^{-1} \tag{46}$$

and

$$\begin{aligned} [A_{ij}] &= \left[-\frac{\partial f_i}{\partial \gamma^p}\frac{\partial \gamma^p}{\partial \mathrm{d}\lambda_j} - \frac{\partial f_i}{\partial p_c}\frac{\partial p_c}{\partial \mathrm{d}\lambda_j} \right] \\ &= \begin{bmatrix} 1 & 1 & \omega \\ 1 & 1 & \omega \\ 2H\overline{p}_c \sin\psi_m & 2H\overline{p}_c \sin\psi_m & 4H\overline{pp}_c \end{bmatrix}, \end{aligned} \tag{47}$$

with superscript -1 denoting the inversion of a matrix.

Finally, this elastoplastic stiffness matrix is transformed from principal stress space to generalized stress space by means of transforming approach mentioned in Section 4, making use of updated total strain tensor, as "STRAN + DSTRAN" in Fortran code.

7. Single element verification

The data of loose Hostun sand from Schanz et al. (1999)'s original work is used here to verify the Hardening Soil model implemented just now. Parameters of the user-defined material is listed in Table 2.

In element tests for oedometer and triaxial tests, the model is established in axisymmetric space and consists of

Table 2 Parameters of loose Hostun sand for Hardening Soil model (Schanz *et al.* 1999)

E_{50}^{ref} [kPa]	E_{oed}^{ref} [kPa]	E_{ur}^{ref} [kPa]	v	c [kPa]	φ [°]	ψ [°]	m	Others
20000	16000	60000	0.20	0.1	34	0.1	0.65	Default values

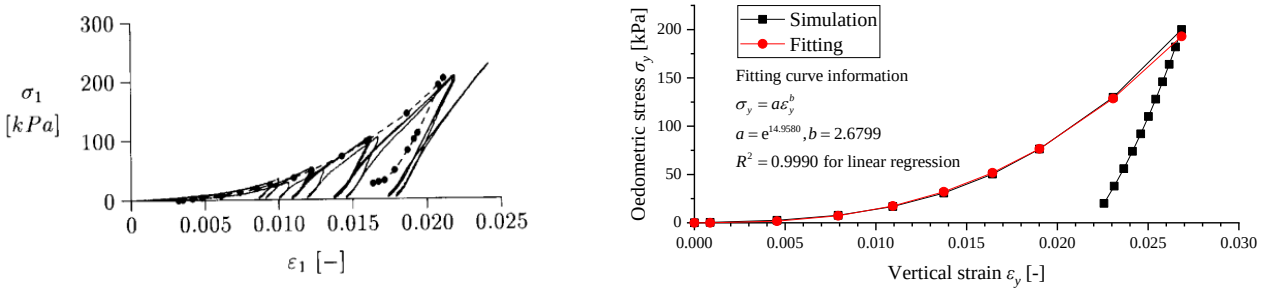

(a) Original simulation and test data after Schanz *et al.* (1999)

(b) Simulation and fitting loading curve after HS model implemented in this paper

Fig. 6 Comparison between original Hardening Soil model and the generalized one implemented in this paper: oedometer test

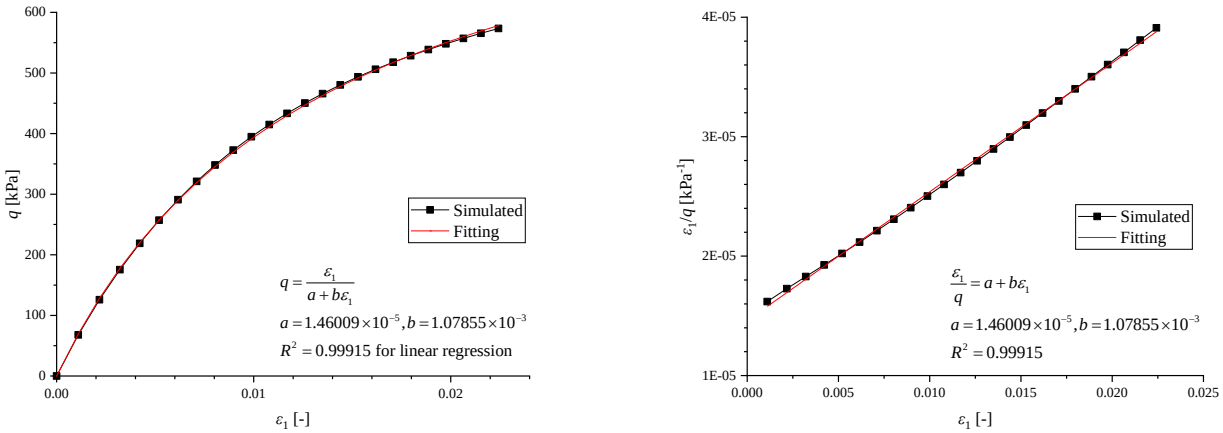

(a) Plot q against ε_1

(b) Plot ε_1/q against ε_1

Fig. 7 Hyperbolic stress-strain curve and its fitting curve

only one square element with both width and height of 1 m, and element type of CAX4.

In simulation of oedometer test, the element is constrained horizontal displacements everywhere, vertical displacements at the bottom and rotation at the axis. A pressure is applied on the top surface of the element, varying under an exponential amplitude to prevent overstraining at the beginning of loading step, since oedometer test curve can be fitted by an exponential function

$$p = p_0 t^{\gamma} \tag{48}$$

where p is the actual pressure, p_0 denotes the reference value of this pressure to be multiplied by amplitude t^{γ}, t is time in a static analysis step whose length is set as 1, and γ is the exponent which is supposed to be greater than 2. By this means the vertical strain increments applied on the element are well averaged.

In analysis of oedometer test p_0 = 200 kPa and γ = 2.7 are chosen, and nonlinear geometry option is not activated.

The resulting curve is compared with Schanz's original simulation in Fig. 6. While the exponent γ = 2.6799 is the best fit to the resulting curve, the ultimate vertical strain is larger for about 0.5%, probably due to the selection of relationships for cap parameters M and H. Because the original Hardening Soil model implemented in Plaxis code is completely based on the concept by Schanz *et al.* (1999), adopting relationships shown in Eqs. (15) and (16) will shift the curve leftwards to fit Schanz's original simulation curve. Almost identical unloading behaviors can be observed in two simulation curves, with vertical strain decreasing for approximately 0.4% from oedometric stress 200 kPa to 20 kPa.

In Schanz's original simulation, the oedometric stress σ_1 is also applied a similar amplitude rather than linear ramping, as observed in Fig. 6(a), especially in early loading period. This prove that an appropriate rule of stress increment during one analysis step is very crucial to total

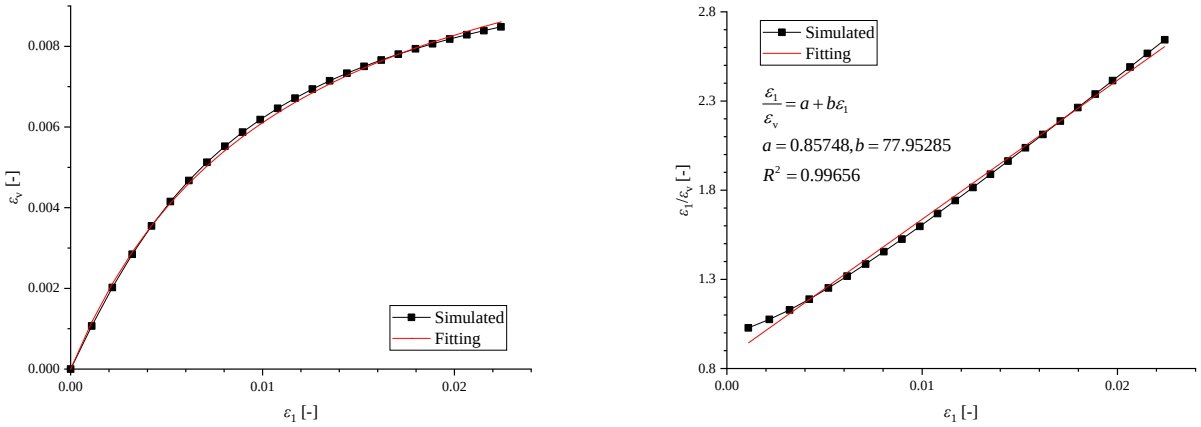

(a) Plot ε_v against ε_1 (b) Plot $\varepsilon_1/\varepsilon_v$ against ε

Fig. 8 Hyperbolic dilation curve and its fitting curve

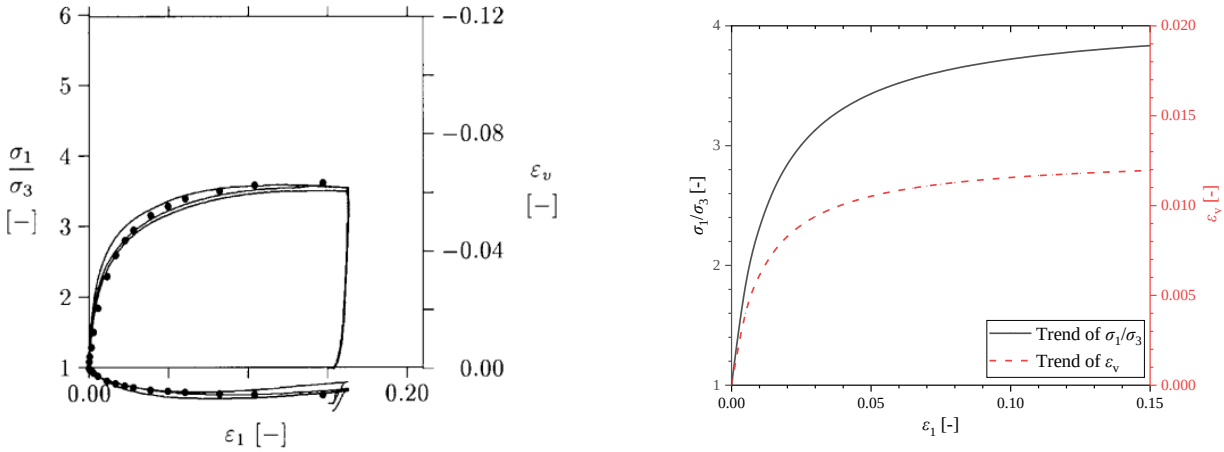

(a) Original simulation and test data after Schanz *et al.* (1999) and Djedid (1986) respectively (b) Trend of stress-strain and dilation curves after HS model implemented in this paper

Fig. 9 Comparison between original Hardening Soil model and the generalized one implemented in this paper: triaxial test

applied stress defined in this step. Otherwise, higher incremental errors due to overstraining will be accumulated to make solution diverge.

The results of undrained triaxial tests under confining pressure σ_3 = 300 kPa, after Djedid (1986) and cited by Schanz *et al.* (1999), are also used to verify the generalized Hardening Soil model in this paper. The basic formulation of Duncan-Chang model is used to amplify the axial stress σ_1 for first diverging trial

$$\Delta\sigma = \sigma_1 - \sigma_3 = \frac{\varepsilon_{1,\max} t}{\frac{2 - R_f}{2E_{50}} + \frac{\varepsilon_{1,\max} t}{q_a}} \tag{49}$$

where $\varepsilon_{1,\max}$ denotes maximum axial strain reached in single test, and E_{50} and q_a are derived from Eqs. (5) and (4) respectively, both keeping constant. The element is constrained vertical displacements at the bottom, as well as horizontal displacements and rotations at the axis. The sole step is defined for primary loading with nonlinear geometry option activated.

A hyperbolic stress-strain curve is yielded after simulation of triaxial test as shown in Fig. 7, which can be described in Duncan-Chang equation

$$\Delta\sigma = \frac{\varepsilon_1}{a + b\varepsilon_1} \tag{50}$$

where a and b are fitting parameters. Though the final convergence of problem is probably controlled by the selection of these two parameters as well as size of increment, the trend of this hyperbolic curve is compared with that after original Hardening Soil model in Fig. 9, where both hyperbolic stress-strain curves coincide considerably well.

The dilation curve is also studied by comparing with results after original simulation, shown in Fig. 8. The curve yielded after the generalized Hardening Soil model implemented in this paper also possesses a hyperbolic shape which is in good agreement with original implementation by Schanz *et al.* (Fig. 9).

The implemented Hardening Soil model is now verified and is applicable to be used in routine design of

geoengineering project. The triaxial and oedometer tests mainly correspond to shear and volumetric hardening of pyramid- and cap-type yield surface, respectively. The simulation of triaxial test reproduces almost perfect hyperbolic stress-strain and dilation curves comparing to those after original model and test data. Though the shapes of initial loading and unloading curves are well derived from simulation of oedometer test, the maximum vertical strain at maximum oedometric stress is a little overestimated probably due to the chosen relationships for cap parameters M and H.

8. Conclusions

With strict respect of hexagonal pyramidal Mohr-Coulomb yield criterion, the popular elastoplastic Hardening Soil model is generalized and redeveloped for finite element analysis code ABAQUS and verified in comparison with original implementation in this paper. Because the model is isotropically hardening, and hence the trial and final stress tensors share the same eigendirection in plastic correction process, the integration process can be performed in principal stress space. First, the governing equations of Hardening Soil model, for both its pyramidal and cap-type yield surface, are strictly adapted to Mohr-Coulomb criterion and therefore generalized in principal stress space. Under Mohr-Coulomb criterion there are six equations for each yield surface as well as plastic flow vectors for shear hardening, depending on six different rankings of principal stress components. The singularities at the corners and apex on Mohr-Coulomb type yield surface are processed via Koiter's rule instead of regular differentiation approach as a result of inconsistent gradients. Along their corresponding directions of plastic flow, the trial stress state is returned simultaneously onto the main and adjacent analytic portions of a yield surface, resulting in a final stress state on the corner. The stress state cannot be returned onto the apex of pyramid since moduli are meaningless there, but in case of isotropic loading it may be returned to the apex of cap-type yield surface where the number of yield equations is reduced to one due to $\tilde{q}=0$. Three equations rather than four are established to return the trial stress state to the intersection point between the corners of pyramid and cap. Ten possibilities of return mapping are thus established for trial stress tensor, together with ten corresponding schemes for assembly of consistent elastoplastic stiffness matrix used for global Newton iteration in ABAQUS code.

The interface for implementation of the Hardening Soil model in ABAQUS code is UMAT (User-defined MATerial) Fortran subroutine. At first, the Cauchy stress tensor is transformed into principal stress space by means of spectral decomposition before integration, yielding principal stresses and their corresponding eigenprojections. The stress tensor is finally updated by transforming back the principal stress tensor to the new Cauchy stress tensor using these eigenprojections. The scheme of spectral decomposition is also used in transforming elastoplastic stiffness matrix to generalized Cauchy stress space, needing the eigensystem of final total strain tensor. Ranking of principal stress components should be also paid attention in axisymmetric and plane strain problems.

The implemented model is verified in element tests for simulating oedometer and triaxial tests. In simulation of oedometer test it can be observed that the selection of relationships for cap parameters may have a significant influence on the ultimate vertical strain at maximum oedometric stress. The ultimate vertical strain can be overestimated for 0.5% with regard of the original Hardening Soil model. On the other hand, the shapes of primary loading and unloading curves are reproduced well, especially the latter since linear elasticity is assumed in unloading process. The hyperbolic stress-strain and dilation curves after simulation of triaxial test are shown to be in almost perfect agreement with original simulation results since all factors of pyramidal yield surface are well defined. It can also be found that the arrangement of stress increments by means of amplitude in ABAQUS code mostly influences the convergence of final solution for these curves.

Acknowledgments

The research work described herein was funded by the National Natural Science Foundation of China (Grant No. 51979122).

References

Abbo, A.J., Lyamin, A.V., Sloan, S.W. and Hambleton, J.P. (2011), "A C2 continuous approximation to the Mohr-Coulomb yield surface", *Int. J. Solids Struct.*, **48**, 3001-3010. https://doi.org/10.1016/j.ijsolstr.2011.06.021.

Amat, S., Levin, D., Ruiz-Alvarez, J. and Yanez, D.F. (2023), "A new B-spline type approximation method for non-smooth functions", *Appl. Math. Lett.*, **141**, 108628. https://doi.org/10.1016/j.aml.2023.108628.

Argani, L.P. and Gajo, A. (2021), "A new isotropic hyper-elasticity model for enhancing the rate of convergence of Mohr-Coulomb-like constitutive models and application to shallow foundations and trapdoors", *Comput. Geotech.*, **132**, 103957. https://doi.org/10.1016/j.compgeo.2020.103957.

Bentley Systems Inc. (2022), *PLAXIS CONNECT Edition V22.01 Material Models Manual*, Bentley Systems Inc., Exton, PA, USA.

Benz, T. (2007), "Small-strain stiffness of soils and its numerical consequences", Ph.D. Dissertation, Universitaet Stuttgart, Germany.

Bolton, M.D. (1986), "The strength and dilatancy of sands", *Geotechnique*, **36**(1), 65-78. https://doi.org/10.1680/geot.1986.36.1.65.

Dassault Systemes Simulia Corp. (2019), *SIMULIA User Assistance 2020*. Dassault Systemes Simulia Corp., Johnston, RI, USA.

De Souza Neto, E.A., Peric, D. and Owen, D.R.J. (2008), *Computational Methods for Plasticity: Theory and Applications*, John Wiley and Sons Ltd, Chichester, United Kingdom.

Djedid, A. (1986), "Etude du comportement non-draine du sable", in *Memoire de D.E.A.*, Institut de Mecanique de Grenoble, Grenoble, France. (in French)

Jaky, J. (1944), "The coefficient of earth pressure at rest", *J. Soc. Hungarian Architects Eng.*, **7**, 355-358.

Jia, S.P., Chen, W., Yang, J.P. and Chen, P.S. (2010), "An elastoplastic constitutive model based on modified Mohr-Coulomb criterion and its numerical implementation", *Rock Soil Mech.*, **31**(7), 2051-2058.

Kawa, M., Puła, W. and Truty, A. (2021), "Probabilistic analysis of the diaphragm wall using the hardening soil-small (HSs) model", *Eng. Struct.*, **232**, 111869. https://doi.org/10.1016/j.engstruct.2021.111869.

Koiter, W.T. (1953), "Stress-strain relations, uniqueness and variational theorems for elastoplastic materials with singular yield surface", *Q. Appl. Math.*, **11**, 350-354.

Lester, A.M. and Sloan, S.W. (2018), "A smooth hyperbolic approximation to the Generalised Classical yield function, including a true inner rounding of the Mohr-Coulomb deviatoric section", *Comput. Geotech.*, **104**, 331-357. https://doi.org/10.1016/j.compgeo.2017.12.002.

Li, C., Li, C., Zhao, R. and Zhou, L. (2021a), "A strength criterion for rocks", *Mech. Mater.*, **154**, 103721. https://doi.org/10.1016/j.mechmat.2020.103721.

Li, C., Li, C. and Zheng, H. (2021b), "Subspace tracking method for non-smooth yield surface", *Comput. Math. Appl.*, **90**, 125-134. https://doi.org/10.1016/j.camwa.2021.03.012.

Mahetaji, M., Brahma, J. and Vij, R.K. (2023), "A new extended Mohr-Coulomb criterion in the space of three-dimensional stresses on the in-situ rock", *Geomech. Eng.*, **32**(1), 49-68. https://doi.org/10.12989/gae.2023.32.1.049.

Matsuoka, H. and Nakai, T. (1985), "Relationship among Tresca, Mises, Mohr-Coulomb and Matsuoka-Nakai failure criteria", *Soils Found.*, **25**(4), 123-128. https://doi.org/10.3208/sandf1972.25.4_123.

Menetrey, P. and Willam, K. (1995), "Triaxial failure criterion for concrete and its generalization", *ACI Struct. J.*, **92**(3), 311-318.

Peric, D. and de Souza Neto, E.A. (1999), "A new computational model for Tresca plasticity at finite strains with an optimal parametrization in the principal space", *Comput. Method. Appl. M.*, **171**(3), 463-489. https://doi.org/10.1016/S0045-7825(98)00221-7.

Pramthawee, P., Jongpradist, P. and Kongkitkul, W. (2011), "Evaluation of hardening soil model on numerical simulation of behaviors of high rockfill dams", *Songklanakarin J. Sci. Technol.*, **33**(3), 325-334.

Pramthawee, P., Jongpradist, P. and Sukkarak, R. (2017), "Integration of creep into a modified hardening soil model for time-dependent analysis of a high rockfill dam", *Comput. Geotech.*, **91**, 104-116. http://dx.doi.org/10.1016/j.compgeo.2017.07.008.

Schanz, T., Vermeer P.A. and Bonnier, P.G. (1999), "The hardening soil model: formulation and verification", *Proceedings of the Beyond 2000 in Computational Geotechnics - 10 Years of PLAXIS*, Balkema, Rotterdam, the Netherlands.

Sui, C.Y., Shen, Y.S., Wen, Y.M. and Gao B. (2021), "Application of the modified Mohr-Coulomb yield criterion in seismic numerical simulation of tunnels", *Shock Vib.*, article ID 9968935. https://doi.org/10.1155/2021/9968935.

Sukkarak, R. Likitlersuang, S., Jongpradist, P. and Jamsawang, P. (2021), "Strength and stiffness parameters for hardening soil model of rockfill materials", *Soils Found.*, **61**, 1597-1614. https://doi.org/10.1016/j.sandf.2021.09.007.

Surarak, C., Likitlersuang, S., Wanatowski, D., Balasubramaniam, A., Oh, E. and Guan, H. (2012), "Stiffness and strength parameters for hardening soil model of soft and stiff Bangkok clays", *Soils Found.*, **52**(4), 682-697. http://dx.doi.org/10.1016/j.sandf.2012.07.009.

Sukkarak, R., Pramthawee, P. and Jongpradist, P. (2017), "A modified elasto-plastic model with double yield surfaces and considering particle breakage for the settlement analysis of high rockfill dams", *KSCE J. Civil Eng.*, **21**(3), 734-745. https://doi.org/10.1007/s12205-016-0867-9.

Sukkarak, R., Pramthawee, P., Jongpradist, P., Kongkitkul, W. and Jamsawang, P. (2018), "Deformation analysis of high CFRD considering the scaling effects", *Geomech. Eng.*, **14**(3), 211-224. https://doi.org/10.12989/gae.2018.14.3.211.

Wang, C., Ding, W. and Qiao, Y. (2014), "Development and application of hardening soil constitutive model in FLAC3D", *Chinese J. Rock Mech. Eng.*, **33**(1), 199-208. https://doi.org/10.13722/j.cnki.jrme.2014.01.015. (in Chinese)

Wang, Z. (2020), "A modified Mohr-Coulomb criterion for rocks with smooth tension cutoff", *Proceedings of the IOP Conf. Ser.: Earth Environ. Sci.*, **525**, 012027. https://doi.org/10.1088/1755-1315/525/1/012027.

Woo, S.I. (2023), "Critical state-based Mohr-Coulomb bounding surface model for sand under monotonic shearing", *Adv. Civil Eng.*, article ID 8703610. https://doi.org/10.1155/2023/8703610.

Wu, X. and Vanapalli, S.K. (2022), "Three-dimensional modeling of the mechanical behavior of a single pile in unsaturated expansive soils during infiltration", *Comput. Geotech.*, **145**, 104696. https://doi.org/10.1016/j.compgeo.2022.104696.

Zhang, S., Wang, Q. and Zhou, W. (2019), "Implementation of the Tresca yield criterion in finite element analysis of burst capacity of pipelines", *Int. J. Pressure Vessels Piping*, **172**, 180-187. https://doi.org/10.1016/j.ijpvp.2019.03.037.

Zienkiewicz, O.C. and Pande, G.W. (1977). "Some useful forms of isotropic yield surfaces for soil and rock mechanics", *Finite Element in Geomechanics*, Balkema, Rotterdam, the Netherlands, 179-190.

CC